Ultra-Strong Regenerated Wool Keratin Fibers Regulating via Keratin Conformational Transition

Liang Zhang, Ning Ma, Xiangzheng Jia, Tianjiao Hua, Jin Zhu, Chenbin Ding, Dongzi Yang, Jinrong Luo, Menglei Wang, Jiajun Luo, Shuo Li, Xiaoling Tong, Qiyue Fan, Zhou Xia, Yanyan Shao, Muqiang Jian, Enlai Gao,* Yuanlong Shao,* and Jin Zhang*

By virtue of remarkable biocompatibility and their promising applications in biomedical fields, biomass-regenerated fibers, such as wool keratin fiber and cellulose fiber, have attracted extensive attention. However, the insufficient mechanical performance still hinders their yarn manufacturing capability and further large-scale applications. Herein, an ultra-strong and ultra-tough regenerated wool keratin fiber by regulating keratin conformation with high-quality small-size graphene (HQSGr) and mechanical training treatment (M-HQSGr-RWKF) is fabricated. With the assistance of mechanical training, a small addition of HQSGr (0.1 wt.%) remarkably augments the secondary structure transition from α-helix to β-sheet of the keratin, which delivers a tensile strength of 215.4 $\pm$ 5.2 MPa, surpassing all reported natural wool and regenerated wool or even poultry fibers. Benefiting from the excellent mechanical strength, wet-state toughness (158.9 MJ m^{-3}), and recoverable strain (205.0%), M-HQSGr-RWKF has been demonstrated as a biocompatible artificial muscle to drive the biomimetic motion, which manifests ultrahigh actuation strain greater than 100.0% and stress of 16.7 MPa. The derived ultra-strong and ultra-tough keratin fiber opens a new avenue for developing smart fiber from biomass resources.

1. Introduction

Environmental concerns and strikingly rising oil prices have driven the booming demand on eco-friendly regenerative biomaterials as replacements for million tons of petrochemical products,[1,2] such as plastics and synthetic fibers.[3,4] As a representative category of regenerative biomaterials, biopolymeric nanofibrils including cellulose in plants,[5–7] bacteria,[8] chitin in crabs,[9,10] keratins in spider silk,[11] silkworm silk,[12,13] wool,[14] and collagen in mammalian ligaments or other organs,[15] could serve as universal nano-building blocks for premium regenerated bio-fiber production according to their wide availability, sustainability, and biocompatibility.[16–19] These biopolymeric nanofibrils usually present analogous structural specialties, reassembling the nanofibrils into sophisticated meso-architecture with controllable

L. Zhang, T. Hua, C. Ding, D. Yang, J. Luo, M. Wang, S. Li, X. Tong,
Q. Fan, Z. Xia, Y. Shao
College of Energy Soochow Institute for Energy and Materials
Innovations (SIEMIS)
Jiangsu Provincial Key Laboratory for Advanced Carbon Materials
and Wearable Energy Technologies
Soochow University
Suzhou 215006, P. R. China
L. Zhang, J. Zhu, Y. Shao
School of Materials Science and Engineering
Peking University
Beijing 100871, P. R. China
E-mail: shaoyuanlong@pku.edu.cn
L. Zhang, N. Ma, J. Zhu, M. Jian, Y. Shao, J. Zhang
Beijing Graphene Institute (BGI)
Beijing 100095, P. R. China
E-mail: jinzhang@pku.edu.cn

X. Jia, E. Gao
Department of Engineering Mechanics
School of Civil Engineering
Wuhan University
Wuhan 430072, P. R. China
E-mail: enlaigao@whu.edu.cn
J. Zhu, J. Luo, Y. Shao
Academy for Advanced Interdisciplinary Studies
Peking University
Beijing 100871, P. R. China
J. Zhang
Center for Nanochemistry
Beijing Science and Engineering Center for Nanocarbons
Beijing National Laboratory for Molecular Sciences
College of Chemistry and Molecular Engineering
Peking University
Beijing 100871, P. R. China

**ADVANCED
SCIENCE NEWS**

www.advancedsciencenews.com

**ADVANCED
FUNCTIONAL
MATERIALS**

www.afm-journal.de

orientation and crystallinity could result in regenerated keratin fibers with novel engineering material designs and consequent exceptional mechanical properties.[20–24]

Wool is a noteworthy keratinous fiber, which is the most important animal fiber used in textile applications by far.[14] More than 2.5 million tons of wool are produced annually worldwide mainly from Australia, China, New Zealand, Iran and Argentina.[25,26] Simultaneously, a large number of waste wool close to the annual wool production were produced from shearing/weaving trimmings, discarded low grade coarse wool, and fast fashion industry.[27] However, based on current wool waste treatment industry, such a tremendous number of keratin-rich biomaterials are mainly treated as low-value feed additives, cosmetic ingredients and waste water treatment agents, or even directly end up in landfill or incineration.[28–30] Recently, producing regenerated fibers from wool keratin (WK) offers a novel and effective high-value strategy for the disposal of waste wool, leading to a significant reduction in carbon footprint, making it a highly sustainable and eco-friendly strategy.[31–35] Owing to the typical knotting/weaving process and abrasion/stretching requirement for textile products, there is a series of rigorous mechanical requirements for fibers applied in textile industry, such as acceptable tensile strength, sufficient strain-to-failure (above 10%), and elastic modulus between 30 and 60 g per denier (3.4–6.8 GPa).[36,37] The current limited tensile strength of ≈137 MPa is still far from satisfying the mechanical requirement for yarn manufacturing and textile industry.[34] WK materials exhibit a complex hierarchical structure, across from nanoscale polypeptide chains, intermediate keratin filaments, microscale aggregates, to macroscale compact sheaths, porous cores, and linear threads.[38,39] Although the complicated hierarchical structure brings great difficulties to reconstruct the biomass fibers, the keratin fibrils could also be an efficient building block for assembling fiber with high mechanical strength.[40–43] Therefore, engineering the keratin fibril structure remains an attractive strategy to build regenerated wool keratin fiber (RWKF) with high mechanical performance for meeting the industrial manufacturing demand.[44–47]

By virtue of its atomically thin structure and conspicuous mechanical performance, graphene has widely been used as a reinforcement for bio-composite fibers.[48–56] However, the underlying reinforcement mechanism, such as the graphene-induced conformation transitions and their effects on fiber mechanical behaviors, has been seldom discussed. Herein, we fabricated an ultra-strong and ultra-tough RWKF by regulating keratin conformation with small addition (0.1 wt.%) of high-quality small size graphene (HQSGr) and mechanical training treatment (M-HQSGr-RWKF). The HQSGr triggers the conformation transition of keratins onto graphene within a distance of ≈12.1 nm that is much larger than the thickness of graphene (0.3 nm). Such a wide range of keratin conformation transition from α-helix to β-sheet and thereafter mechanical training induced alignment and densification of these structures remarkably enhance the mechanical performance of RWKF. Benefiting from the ultrahigh strength, wet-state toughness, and recoverable strain, the M-HQSGr-RWKF has been assembled into a fiber-shaped biocompatible artificial muscle with ultrahigh actuation strain (>100.0%) and stress (16.7 MPa), outperforming the state-of-the-art biomaterial derived systems.[57–60]

2. Results and Discussion

2.1. Continuous Preparation of M-HQSGr-RWKF via Wet-Spinning

Figures 1A and S2C, Supporting Information, schematically illustrate the wet-spinning preparing process and the continuous evolution from keratin fibril dispersion into M-HQSGr-RWKF. First, only small addition of HQSGr (0.1 wt.%) flakes have been uniformly mixed in the WK dispersion while preparing wet-spinning doge. Surfactants such as sodium dodecyl sulfate (SDS) have been added into wet-spinning dispersion to introduce electrostatic repulsive force to assist HQSGr flakes dispersion in alkalescent $Na_2CO_3/NaHCO_3$ liquid. Simultaneously, we also optimized the keratin extraction and pure RWKF wet-spinning process to guarantee high-quality matrix fiber for deep reinforcement. As illustrated in **Figure 1**A, directed by fluid-induced shear force, the HQSGr flakes tend to align along the flow direction, especially when the mixed dispersion flows through the narrow spinneret space. In this regard, the aligned HQSGr flakes constructed layered confinement space to intensify the orientation of keratin fibril conformation and even crystallinity transition from α-helix to β-sheet onto graphene within a certain distance. The re-constructing of disulfide bonds during the oxidation bath, combined with the continual stretching of the keratin fibril chains during the mechanical training treatment, finalized in the compact M-HQSGr-RWKF with ultrahigh mechanical performance.

Figure S2B, Supporting Information, depicts the massive production of M-HQSGr-RWKF and pure RWKF with hundreds of meters in length via a consistent continuous wet-spinning technique (yield speed of ≈700 m h^{-1}). The scanning electron microscopes (SEM) diagrams in Figure 1B shows that, after continuous mechanical training treatment, the M-HQSGr-RWKF still exhibits an analogical smooth surface and an approximate diameter of 30 μm compared with the well-definite RWKF. Furthermore, the M-HQSGr-RWKF exhibits remarkable flexibility and high mechanical strength, as evidenced by its ability to be tightly tied into knots. To explore the mechanical properties of pure RWKF, HQSGr-RWKF, and M-HQSGr-RWKF in detail, we resolve the stress-strain curves in Figure 1C. In general, all of RWKF, HQSGr-RWKF, and M-HQSGr-RWKF present an elastic deformation at the initial tensile process. After the stress reaches the yield strength, the fiber depicts a conspicuous plastic deformation. The thus-derived M-HQSGr-RWKF manifests a tensile strength of 215.4 ± 5.2 MPa and a strain-to-failure of 8.8 ± 0.9%, surpassing those of HQSGr-RWKF (strength of 181.4 ± 12.6 MPa and strain-to-failure of 10.5 ± 0.9%) and RWKF (strength of 120.8 ± 9.3 MPa and strain-to-failure of 11.3 ± 1.8%) prepared with the same wet-spinning parameters. Furthermore, the other mechanical properties, including Young's modulus, toughness, and weight-bearing ratio (the ratio of the weight that fiber can afford to its own weight) are compared (Figure 1D). M-HQSGr-RWKF, HQSGr-RWKF, and RWKF exhibit toughness of 12.9, 10.6, and 9.0 MJ m^{-3}, Young's moduli of 6.1, 3.2, and 1.7 GPa, and weight-bearing ratios of 2.0×10^3, 1.5×10^3, and 1.0×10^3, respectively. These results indicate the simultaneous improvement in strength, toughness, and modulus of M-HQSGr-RWKF.

ADVANCED
SCIENCE NEWS

www.advancedsciencenews.com

ADVANCED
FUNCTIONAL
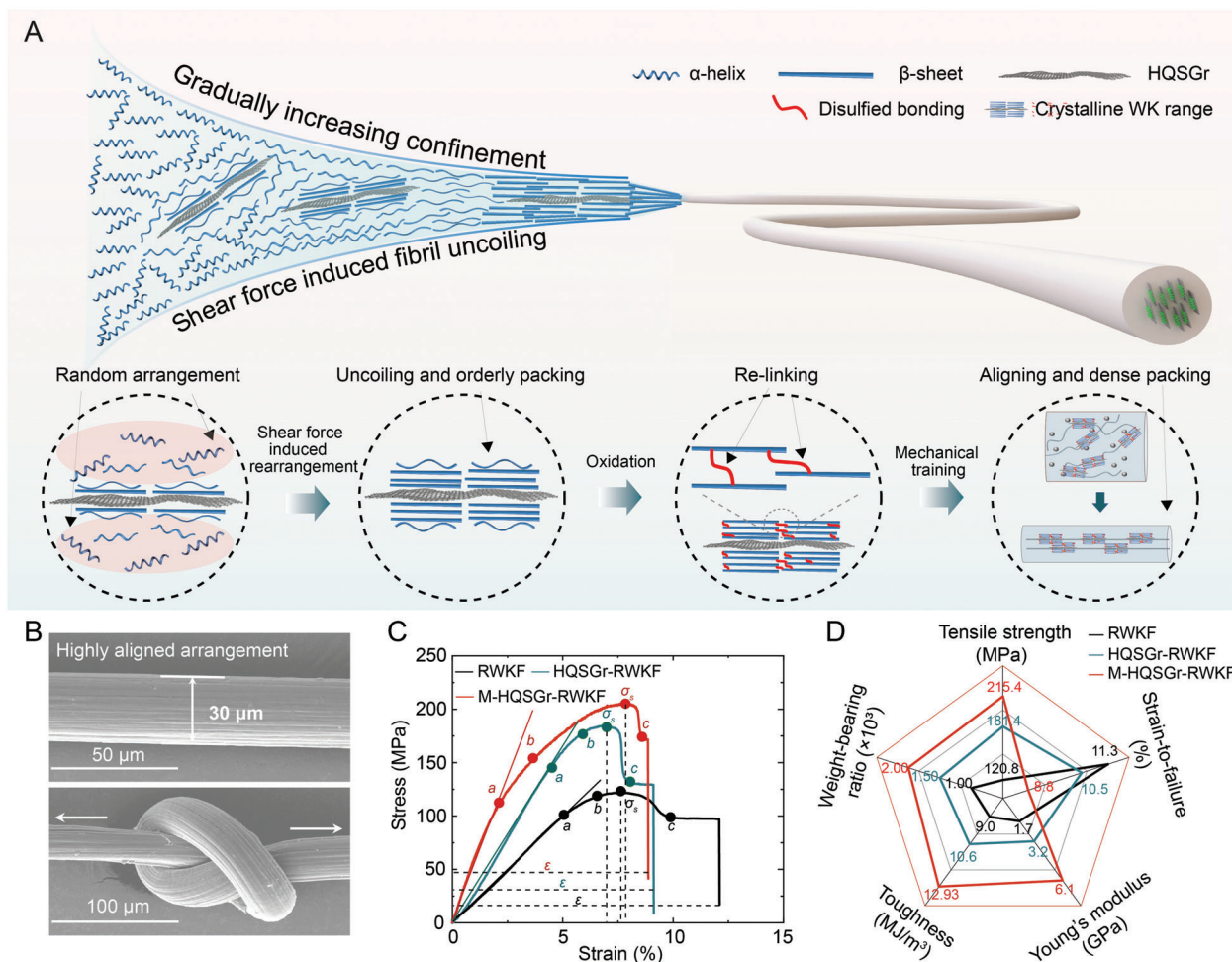**MATERIALS**

www.afm-journal.de

Figure 1. Continuous preparation of M-HQSGr-RWKF. A) Schematic illustration of the M-HQSGr-RWKF wet-spinning process. The magnified graphic highlights the interaction between keratin fibril and HQSGr during the wet-spinning and mechanical training post-treatment. B) Front-surface SEM images of the straight and knotted M-HQSGr-RWKF. C) Stress-strain curves of M-HQSGr-RWKF, HQSGr-RWKF, and RWKF. *oa*: the linear elastic region; *ab*: the nonlinear elastic region; *bc*: the yield region, where ϵ is the strain-to-failure, σ_s is the tensile strength. D) Mechanical performance comparison of M-HQSGr-RWKF, HQSGr-RWKF, and RWKF, including tensile strength, strain-to-failure, Young's modulus, toughness, and weight-bearing ratio.

2.2. Template Effect of HQSGr on Keratin Conformation Transition

The classical theory of composite mechanics is inadequate to explain the substantial enhancement of mechanical performance of M-HQSGr-RWKF via such a small addition of HQSGr (see Text S1, Supporting Information for details). Generally, there are two critical factors to endow the graphene with significant reinforcement effect, i.e., graphene/keratin interaction in wet-spinning doge solution phase and graphene/keratin conformation transition during the wet-spinning process. To elaborate the reinforcement mechanism for optimal design, a series of graphene materials, including small-size graphene oxide (SGO), small-size reduced graphene oxide (SRGO), and large-size graphene (LGr), have been introduced to analyze the effects of surface functionality and size on graphene/keratin interaction (Figures S4, S5, S6, and S7, Supporting Information).

The adsorptions of keratin onto different graphene surfaces were verified from the observation of electron transitions. Amino acids containing benzene rings (tyrosine, tryptophan, and phenylalanine) undergo electronic transitions when excited by ultraviolet (UV) light and reflected at 280, 275, and 250 nm, respectively. The UV-vis spectra in Figure S8A, Supporting Information, depict evident absorption peak intensity annihilation and blue shift of the peak centered at the specific wavelength of ≈245 nm. It corresponds to the strong π–π conjugation between the amino acid and the graphene, which inhibits the electronic transition of the benzene ring. Fluorescence quenching is a powerful technique in the field of researching the dynamic changes of keratin structure in complex systems.[61–63] The remarkable fluorescence quenching effect in fluorescence spectra further supports the adsorption of keratin onto HQSGr (Figure S8B, Supporting Information). In summary, the HQSGr could serve as an ideal reinforcement phase to build the solid and compact interaction with keratin fibrils.

To provide insight into the structural evolution of keratins, we did atomistic simulations by placing an α-helix on the monolayer graphene. During the structural equilibrium for a
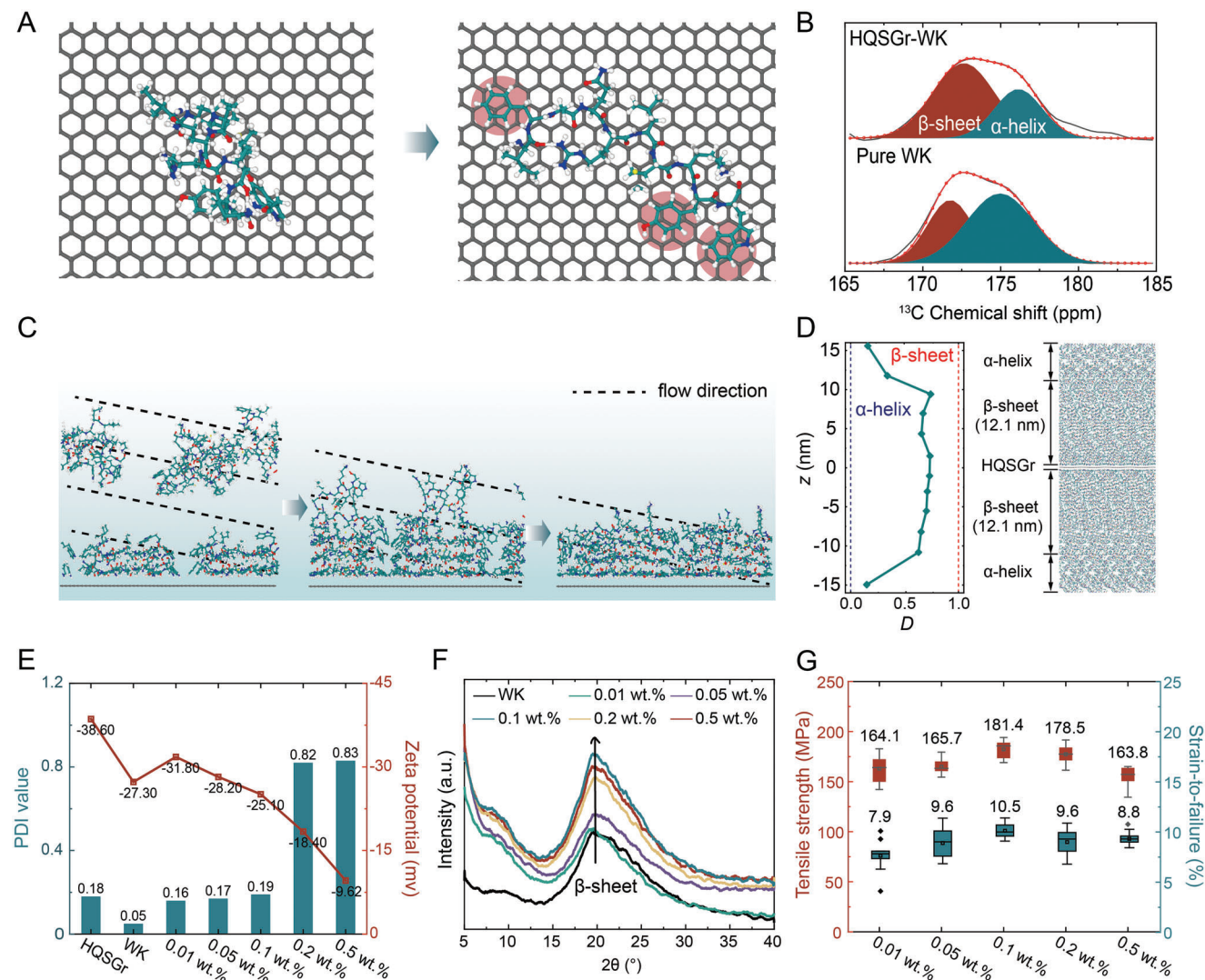
ADVANCED
SCIENCE NEWS
www.advancedsciencenews.com

ADVANCED
FUNCTIONAL
MATERIALS
www.afm-journal.de

Figure 2. Graphene Surface functionality and size effects on graphene/keratin interaction. A) Structure evolution of α-helix onto graphene before and after the room temperature (300 K) equilibrium. B) Deconvolved ^{13}C NMR spectra comparison between pure WK and HQSGr-WK hybrid dispersion in a specific range to illustrate the ratio of α-helix and β-sheet. C) Illustration for the flow-assisted ordered arrangement of keratin onto graphene. D) Transition degree and a snapshot of keratins affected by a graphene sheet. E) Zeta potential and PDI values of spinning solutions with different HQSGr ratios. F) XRD pattern of HQSGr-RWKFs with different HQSGr ratios. G) Tensile strength and strain-to-failure of HQSGr-RWKFs with different HQSGr ratios.

duration of 1 ns, this α-helix spontaneously uncoils into β-sheet (**Figure 2**A), in which all benzene rings of the keratin closely overlap onto HQSGr because of their strong π–π interactions. This process is also quantified by the increase in radius of gyration (R_g) (Figure S9, Supporting Information). These results indicate that the π–π interaction is crucial to induce the transition from α-helix to β-sheet. The π–π interaction increases the binding stress on α-helix when keratin absorbs onto graphene, which leads to the simultaneous transition from α-helix to β-sheet. Solid-state nuclear magnetic resonance (NMR) spectroscopy has been conducted to characterize the structural information during the uncoiling of α-helix via characteristic chemical shift peak and its offset. As shown in Figure S10, Supporting Information, the comparison of ^{13}C solid-state NMR spectra revealed that the typical peak centered at 54 ppm is ascribed to β-sheet (or random coil).[64–68] In

addition, the carbonyl resonance located at 173 ppm could be deconvolved into contribution from α-helix and β-sheet, in which β-sheet ratio (herein, the total content of α-helix and β-sheet is defined as 100%) transmits from 37.8% for RWKF to 66.4% for HQSGr-RWKF (Figure 2B), respectively. The significant peak intensity enhancement at 54 ppm and 175 ppm further supports the prominent keratin conformation transition from α-helix to β-sheet after mixing HQSGr flakes in keratin dispersion, which provides experimental evidence to support our simulation findings.

The wet-spinning fluid hydrodynamic shear stress and drafting confinement are the decisive factors to determine the crystallinity and fibril orientation of the resultant fiber. HQSGr flakes tend to form into aligned arrangement while the mixed spinning fluid extruded through the narrow spinneret. Meanwhile,

**ADVANCED
SCIENCE NEWS**

www.advancedsciencenews.com

**ADVANCED
FUNCTIONAL
MATERIALS**

www.afm-journal.de

the adjacent HQSGr flakes could build a confined space to generate shear force to induce specific range of α-helix keratin fibril close to graphene flakes transmit into β-sheet crystalline stacking structure.

To further understand the enhanced mechanical performance of HQSGr-RWKF, we did atomistic simulations and relevant analyses (see Texts S1 and S2, Supporting Information for details). Based on the classical rule of composite material, Young's modulus of HQSGr-RWKF was predicted as 2.3 GPa, which is much lower than the experimental measurements (3.2 GPa). This is because the classical theory only considers the enhancement effect from intrinsic modulus of graphene (see Text S1, Supporting Information for details). In fact, keratins in the HQSGr-RWKF can be divided into amorphous, α-helix and β-sheet regions,[15] and Figure 2A demonstrated that graphene can act as nucleating agents for β-sheet crystallization. Considering the enhancement effect from this graphene-induced β-sheet crystallization, we here propose a modified rule-of-mixture to account for the modulus enhancement, which predicts that the range of β-sheets onto graphene is as high as 9.8 nm (see Text S1, Supporting Information for details) from the experimentally measured modulus. To support this prediction, atomistic simulations were performed to explore the nucleation and growth of β-sheets onto graphene. The simulation of Figure 2A shows the transition from α-helix to β-sheet onto graphene, which indicates the nucleation of β-sheets onto graphene. Moreover, the strategy of flow-directed assembly was adopted during the experiment (Figure 2C). The wet-spinning fluid hydrodynamic shear stress and drafting confinement are the decisive factors to determine the crystallinity and fibril orientation of the resultant fiber. HQSGr flakes tend to form into aligned arrangement while the mixed spinning fluid was extruded through the narrow spinneret. Hence, it can be expected that the flow can accelerate the nucleation and growth of β-sheets onto graphene. We further investigated whether the predicted wide range (9.8 nm) of β-sheet crystallization onto graphene sheet is energetically favorable. Herein, a range ($\approx$17.0 nm) of α-helices were initially placed onto monolayer graphene, and the α-helices close to the graphene sheet were then progressively translated into β-sheets (Figure S12A, Supporting Information). By fully equilibrating these structures, we calculated the potential energy per atom (ΔE) for different ranges of β-sheets onto graphene with respect to that for full α-helices onto graphene. Figure S12B, Supporting Information demonstrates that ΔE first decreases to negative values and then increases to positive values as the range of β-sheets increases. The negative values of ΔE indicate that the transition from α-helices to β-sheets onto graphene at a range up to 12.1 nm is energetically favorable, which generally supports the above-predicted range (9.8 nm) of β-sheet crystallization onto graphene. To further quantify the structural stabilities, the degree of transition (D) was defined as

$$D = \left(l - l_\alpha\right) / \left(l_\beta - l_\alpha\right) \tag{1}$$

where l and l_α represent the end-to-end lengths of keratin and fully equilibrated α-helix, respectively, and $l_\beta - l_\alpha$ is the difference between the lengths of fully uncoiled β-sheet and fully equilibrated α-helix. Upon equilibration at room temperature (300 K), the result indicates that such a wide range of β-sheet crys-

tallization onto graphene can maintain the structural integrity (Figure 2D). To summarize, β-sheets can nucleate and grow onto graphene because of the strong bio-nano interfacial interactions, and the growth of β-sheets onto graphene therein can be accelerated by the flow-directed assembly. Once the assembly is completed, a wide range of β-sheets onto graphene is energetically favorable and the integrity of this structure can be maintained. Therefore, the enhanced modulus of HQSGr-RWKF is attributed to the reinforcement of graphene and β-sheet crystallization onto graphene.

Afterwards, we systematically optimize the addition of HQSGr and investigate its effect on the dispersibility and reinforcement (Figures 2E and S13, Supporting Information). HQSGr with a series of ratios, such as 0.01 wt.%, 0.05 wt.%, 0.1 wt.%, 0.2 wt.%, and 0.5 wt.%, have been mixed in the keratin wet-spinning dispersion to evaluate its dispersibility and reinforcement effect on keratin crystallinity, fibril orientation, and fiber mechanical performance. The sedimentation experiment and Zeta potential characterization have been first utilized to evaluate the dispersibility of the mixed dispersion. After 12 h sedimentation, the HQSGr and WK mixtures (0.01 wt.%, 0.05 wt.%, 0.1 wt.%) present consistent stability. Figures 2E and S13, Supporting Information demonstrate that 0.1 wt.% HQSGr mixed WK dispersion exhibits a Zeta potential of −25.10 mV and polydispersity index (PDI) of 0.19, which achieves the maximum graphene content while maintaining the mixture stability. Afterwards, polarizing microscopy has been conducted to monitor the keratin fibril aggregate structure after introducing HQSGr flakes with different ratios. As shown in Figure S14, Supporting Information, the distinct anisotropic birefringence for wet-spinning 0.1 wt.% HQSGr-RWKF indicates its conspicuous keratin fibril orientation. In comparison, 0.5 wt.% HQSGr-RWKF tends to form into stacking flakes at the beginning of wet-spinning, resulting in the edge-only keratin alignment. Figure 2F depicts the X-ray diffraction (XRD) pattern for HQSGr-RWKF with different hybrid HQSGr ratios. 0.1 wt.% HQSGr-RWKF presents the most prominent diffraction peak and the narrowest half peak width located at 19.50°, which corresponds to the crystalline feature of β-sheet. Figures 2G and S15, Supporting Information, summarize the stress-strain curves and mechanical performance of HQSGr-RWKFs with different HQSGr ratios, in which 0.1 wt.% HQSGr-RWKF exhibits the highest tensile strength of 181.4 ± 12.6 MPa with the strain-to-failure of 10.5 ± 0.9%. In addition, the high quality of the graphene within RWKF guarantees a tiny amount of defects and impurities. Considering the toxicity of graphene mainly derived from the impurities, only 0.1 wt.% graphene introduction could seldomly lead to safety issues. Graphene in hybrid fiber mainly distributes in the surrounding of wool keratin fibrils. We believe that the use of the HQSGr in fiber production has significant potential for enhancing fiber properties without posing underlying health and safety risks.

2.3. Mechanical Training Post-Treatment

Mechanical "muscle" training treatment has been confirmed as an efficient strategy to achieve the tensile strength enhancement.[69–71] With mimicking the self-growing mechanism of muscle training, repetitive polymer chain stretching and
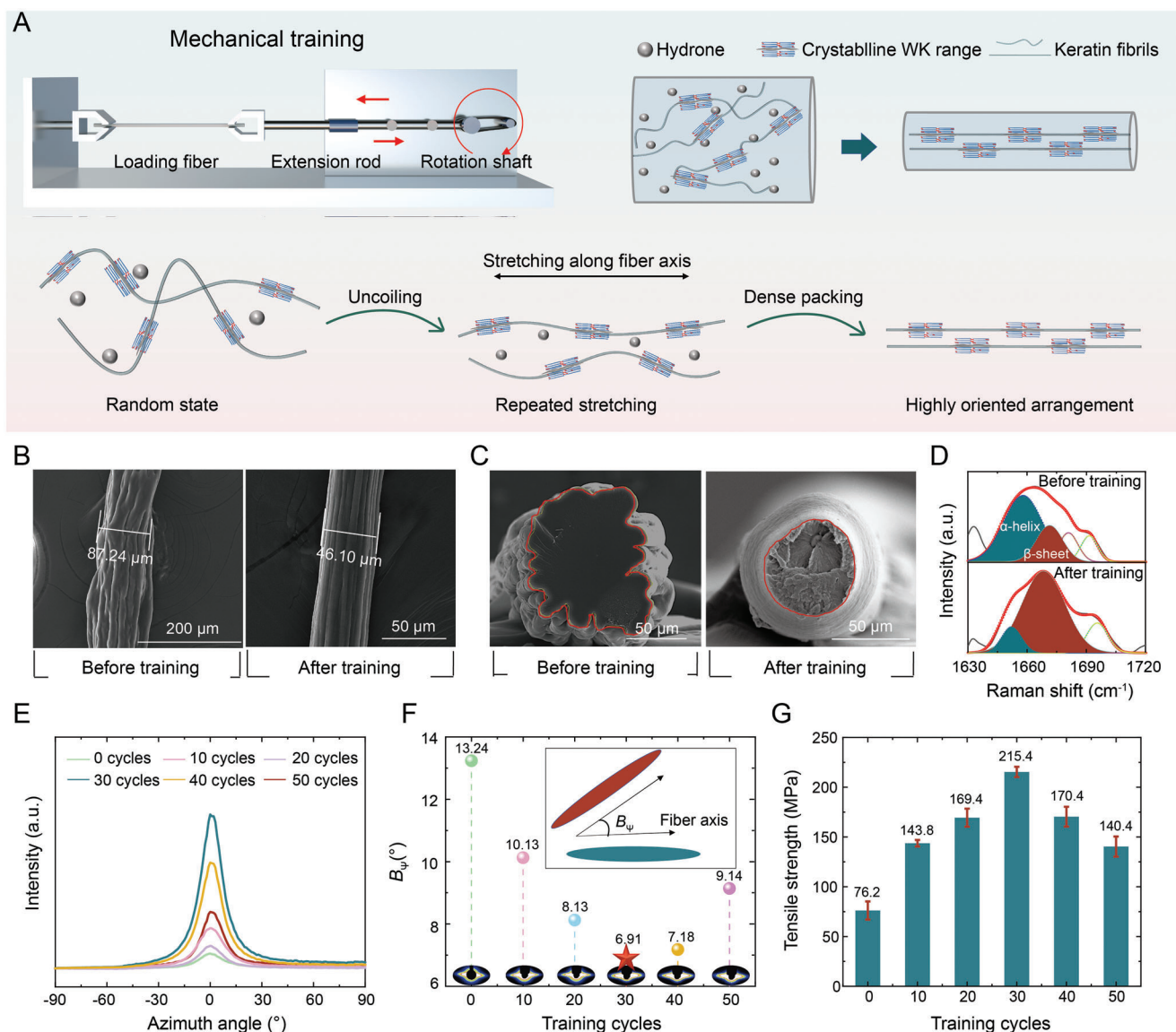
**ADVANCED
SCIENCE NEWS**

www.advancedsciencenews.com

**ADVANCED
FUNCTIONAL
MATERIALS**

www.afm-journal.de

Figure 3. Mechanical training reinforcement mechanism of M-HQSGr-RWKF. A) Schematic diagram of mechanical training mechanism of M-HQSGr-RWKF. B, C) SEM images of the hybrid keratin fiber before and after mechanical training. D) Deconvolved Raman spectra of HQSGr-RWKF before and after continuous mechanical training. E) The relationship between azimuth angle and intensity under different training cycles. F) Summary of B_Ψ orientation distribution of the M-HQSGr-RWKF after different training cycles. The inset illustration explains the meaning of B_Ψ. G) Tensile strength summary of M-HQSGr-RWKF with different training cycles.

effective mechanochemical transduction could construct aligned nanofibrillar architectures with even nanocrystalline domains. These microstructure transitions could significantly enhance the mechanical strength of the trained fiber. As such, the mechanical training post-treatment is implemented to enhance the mechanical strength of the wet-spinning regenerated wool keratin fiber (RWKF) and the hybrid keratin fiber. As demonstrated in Figures 3A and S16, Supporting Information, some randomly coiled keratin fibrils in keratin fibers have been stretched and aligned to demonstrate a short-range ordered feature after continuous repeating slack and drafting on our homemade training facility. The repeated drafting could efficiently facilitate the keratin fibril orientation and the transition from α-helix

to β-sheet. The optical (Figure S17, Supporting Information) and SEM (**Figure 3**B,C, and S18, Supporting Information) images demonstrate that rough and loose-packing hybrid keratin fiber gradually turns into a smooth and compact configuration, which confirms that the randomly distributed nanofibrils gradually reorient and align toward the stretching direction. Subsequently, upon relaxation of the stretching, the partially aligned nanofibrils will elastically revert back to their prior random distribution, thereby creating additional free volume for subsequent stretching of the fibril chains. As the mechanical training cycle increases, plastic deformation accumulates in the fiber, which gradually elongates along the stretching direction. Simultaneously, the rearrangement of the keratin fibrils could

be also validated through the fiber diameter contracted from 87.24 μm to 46.10 μm, while the mechanically trained fiber also presents a more homogeneous cross-sectional fracture pattern. It further reveals that the nanocrystalline domains in keratin fibrils have been reoriented during the stretching treatment. We also supplement the Raman and Fourier-transform infrared spectroscopy (FT-IR) spectra to analyze the structure transition of the fibril itself. As shown in Figure 3D and S19, Supporting Information, amide I band Raman peak could be deconvoled to distinguish α-helix (1650–1660 cm⁻¹) and β-sheet (1670–1680 cm⁻¹).[72] As the mechanical training cycle extends, the β-sheet contribution gradually increases from 28% to 79% to reach the maximum tensile strength at 30 cycles training. The FT-IR spectra verified the coincident phenomenon of the crystalline domain variation tendency (Figure S20, Supporting Information).

To optimize the mechanical training impact on the mechanical properties of hybrid keratin fiber, we systematically increase the training cycle from 10 to 50 cycles to investigate the evolution of microstructure. Meanwhile, we increase the preset draft ratio (λ) from 1.6 to 2.4 to match the fiber length extension. The keratin fibril alignment reaches a steady state after the training cycle reaches 30. Small angle X-ray scattering (SAXS) has been utilized to semi-quantitatively characterize the fiber orientation (Figure 3E,F). The features (such as shape, size, distribution, and orientation) of the particles (including voids) can be studied by analyzing the SAXS patterns.[73–75] First, the relationship between scattering intensity I and azimuth θ was further analyzed via Fit2D (Figure 3E). As the training cycle increases, the peaks along the prestretched direction become more pronounced, indicating the remarkable improvement in the orientation of keratin fibrils. The diffraction vector q and the reciprocal space vector s can be further obtained via adjusting parameters about Fit2D. Herein, the relationship among parameters is as

$$s = q/2\pi \tag{2}$$

More fundamentally, B_{obs} can be obtained by integrating.[76] B_{obs} is the full width at the half maximum of the azimuthal profile from the equatorial streak, which is related to the orientation and the size of the particles.[77] B_{obs} is defined by

$$B_{obs} = \frac{\int I(s, \varphi)\, d\varphi}{\int I\left(s, \frac{\pi}{2}\right)} \tag{3}$$

Calculate sB_{obs},[75] and then use Origin to conduct linear fit over sB_{obs}. An approximate slope and an intercept can be endowed on this basis. If Gaussian distribution can be used to approximate the orientation distribution of the scatterers, the relationship can be presented as follows

$$sB_{obs}\,(s) = sB_{\psi} + \frac{1}{L} \tag{4}$$

where B_{ψ} is the misorientation angle, which reflects the orientation distribution, and L represents the mean length of the scatterers.[78,79] Through the above calculation method, we obtained B_{ψ} of the fibrils in the M-HQSGr-RWKF (Figure 3F), which reaches the lowest value of ≈6.91° with 30 training cycles. The tensile strength of the M-HQSGr-RWKF reaches the highest value of ≈215.4 ± 5.2 MPa with 30 training cycles (Figure 3G), which is consistent with the azimuth variation trend. Simultaneous fiber strength surpasses all reported natural wool and regenerated wool or even poultry fibers (see Table S1, Supporting Information for details). Therefore, mechanical training post-treatment has been verified as an appropriate strategy to reach a new record tensile strength with nanocrystalline and orientation optimization.

2.4. M-HQSGr-RWKF Artificial Muscle and its Actuating Mechanism

With the efficient capability to complete movements in response to external stimuli, biocompatible actuators have attracted extensive attention in fields of artificial muscle,[80,81] drug delivery,[82] biosensing,[83] and implantable devices.[84] The dynamic switch between the uncoiling of α-helix and the recoiling of metastable β-sheet upon uniaxial strain and humidity regulation endow wool keratin as the effective material to offer the programmable stimuli-responsive actuation capability.[85] As schematically illustrated in **Figure 4**A, WK could serve as the ideal component to assemble biocompatible artificial muscle according to the similar hierarchical filament configuration and the reversible humidity-responsive actuation behavior.[15,57] To provide insight on the structural evolution of keratins, atomistic simulations and relevant analyses have been conducted to reappear the transition between α-helix and metastable β-sheet under strain and moisture environment (Figure 4B, Movie S1 and S2, Supporting Information). The simulation snapshots demonstrate the transition from α-helix to β-sheet under tension, and this process was divided into three stages based on the evolution of relative potential energy of keratin (Figure 4C): I) The hydrogen bonds were broken with the increasing energy. II) The angles between adjacent amino acids were expanded. III) The transition from α-helix to β-sheet was completed, and the loading capacity was conspicuously improved at the meantime. On the other hand, Figure S21, Supporting Information demonstrates the rapid transition from β-sheet to α-helix in water via the evolution of transition degree while β-sheet contacts moisture. These results provide the fundamental picture for transition between α-helix and β-sheet, which account for the actuation of M-HQSGr-RWKF observed in experiments. With anisotropic and oriented keratin fibril assembly architecture, M-HQSGr-RWKF is expected to present remarkable actuation performance with transmitting the structural transition on all spatial scales.

Tensile tests for both RWKF and M-HQSGr-RWKF in a wet state (Figure 4D) were carried out to compare the structural evolution in the configuration stretching and mechanical property transforming process. The reversibility further validates the reversible transition from α-helix to β-sheet. The RWKF and M-HQSGr-RWKF show an initial elastic behavior up to the strain of 18% and 10%, respectively (1.7 GPa and 3.2 GPa for Young's moduli of RWKF and M-HQSGr-RWKF, respectively). This corresponds to the reversible α-helix uncoiling process (black line at the initial range). As the strain increases, the α-helix starts to uncoil due to the elongation of irreversible keratin peptide chains (red line range), which causes the taut chain structure to temporarily relax (the temporary decrease of stress). With the
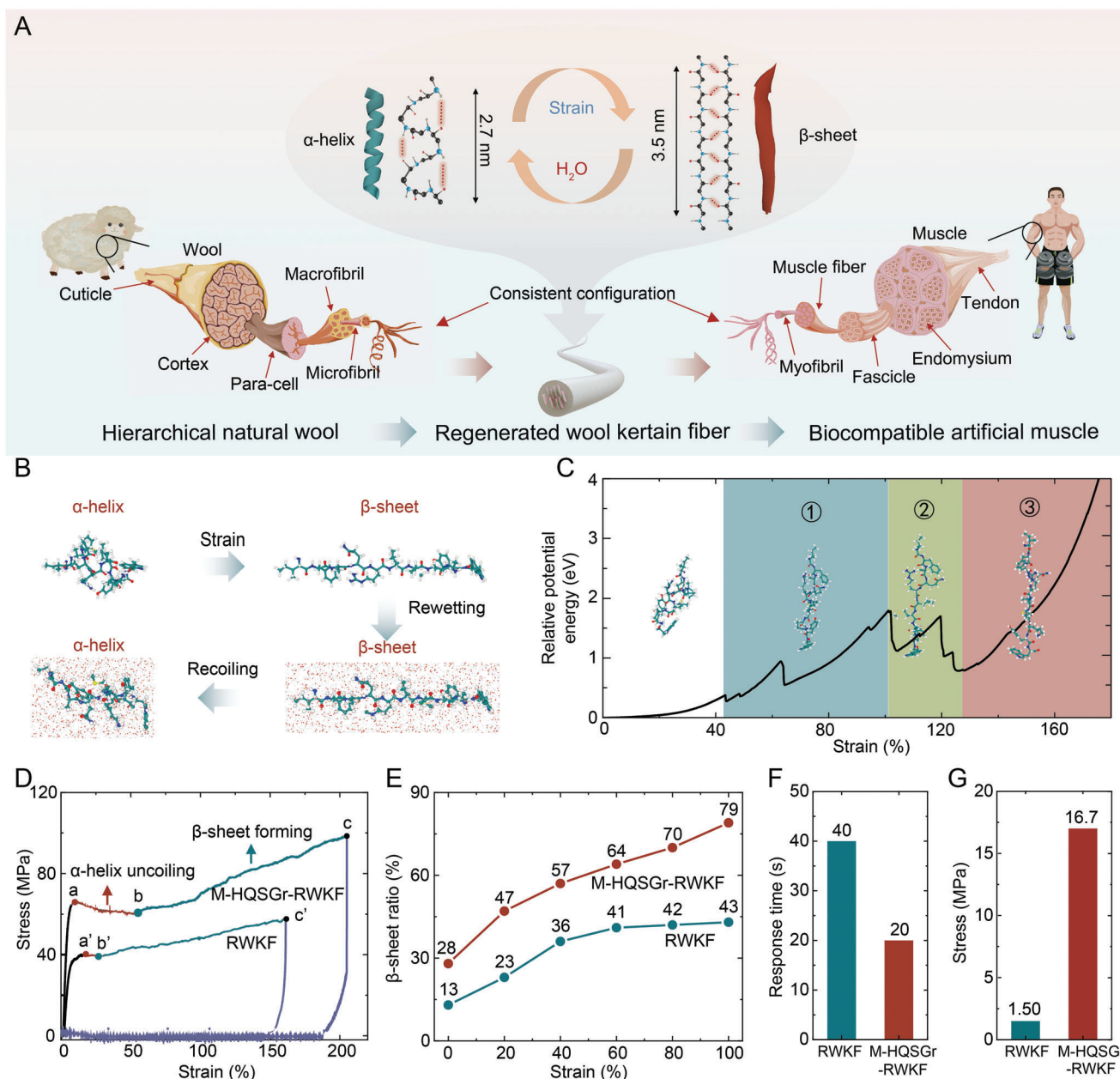
Figure 4. Actuating mechanism of keratin-based fibers. A) Schematic diagram to illustrate the mimicking hierarchical structure from RWKF into biological muscles to produce artificial muscles. B) Atomistic simulation snapshot of the actuation mechanism. The images were collected from Movies S1 and S2, Supporting Information. C) Relative potential energy evolution of keratin from α-helix to β-sheet during the stretching process. D) Stress-strain curves of RWKF and M-HQSGr-RWKF in a wet state. Stress relaxation (ab, $a'b'$ segment) and strain hardening (bc, $b'c'$ segment) ranges are obviously indicated in the curve. E) β-sheet ratio summary for both RWKF and M-HQSGr-RWKF with different strains. F,G) Response time and output stress of both RWKF and M-HQSGr-RWKF.

continuous stretching and the dissipation of moisture, the uncoiled and elongated keratin fibrils maintain stability in their stretched geometry due to the transition from α-helices to β-sheets. The keratin fibrils in RWKF tend to stretch into β-sheets at $\approx$26% strain, corresponding to the strain hardening stage with increasing stress. In contrast, with the addition of HQSGr, M-HQSGr-RWKF manifests a significantly improved stress of 65.2 MPa and an extended α-helix uncoiling process, resulting

in the initiation of β-sheet at $\approx$55% strain and an ultrahigh recoverable strain even beyond $\approx$200%. In this region, the applied stress gradually dissipated via the uncoiling of α-helices and the stretching of β-sheets. The long elastic strain of the M-HQSGr-RWKF is in good agreement with the transition from α-helices to the generated metastable β-sheets. For the recovery process of β-sheets back to α-helices, the inducing extra energy is important to serve as the indispensable entropy power to drive the
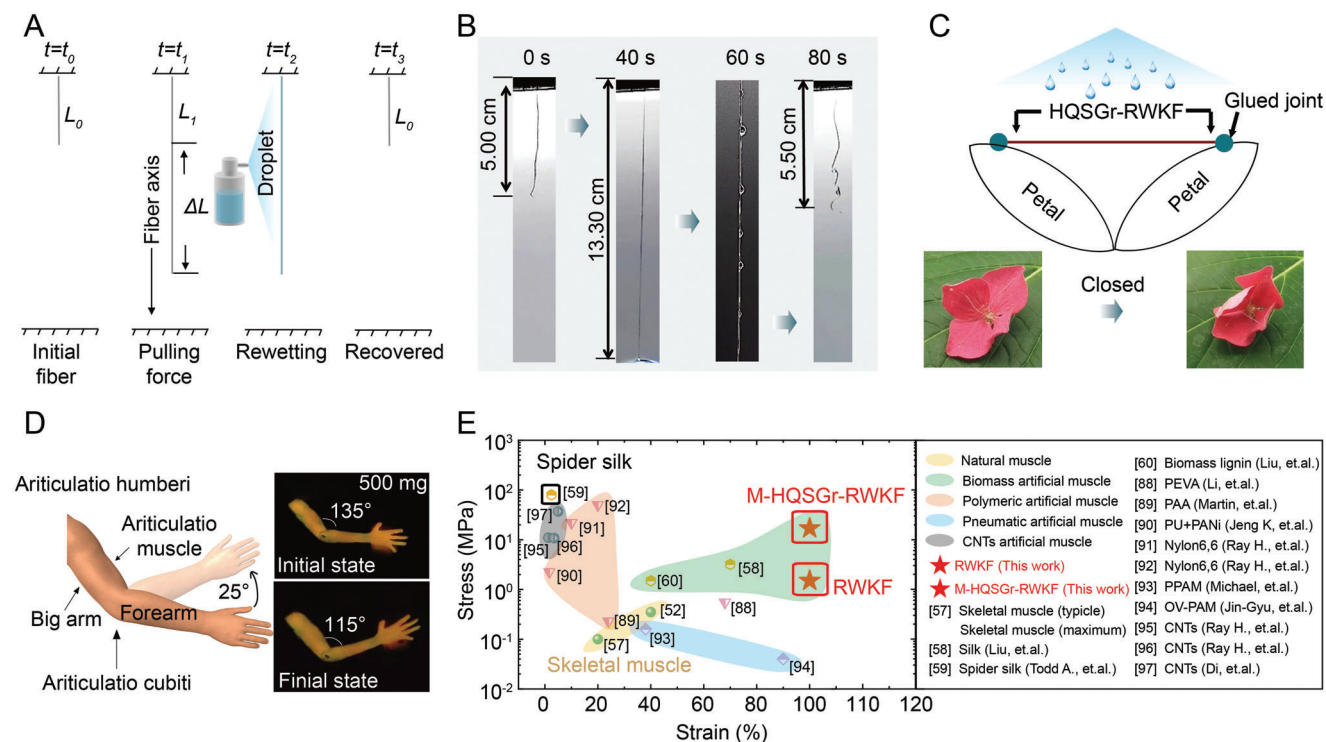
Figure 5. Multi-scene applications of M-HQSGr-RWKF artificial muscle. A) Schematic diagram for the actuation process of M-HQSGr-RWKF. The whole process is divided into four stages, which are recorded at t_0, t_1, t_2, and t_3, respectively. B) Digital photos of fibers from stretch to recovery. The initial fiber length is 5.00 cm, and the maximum fiber length after stretching is 13.50 cm. The M-HQSGr-RWKF could recover to 5.50 cm, with a strain of up to 140%. C) Automatical close of petals under humidity stimulation driven by M-HQSGr-RWKF. The schematic diagrams illustrate the loading form of M-HQSGr-RWKF on petals, and the whole process could be observed detailedly in Movie S3, Supporting Information. D) Schematic demonstration and optical images of forearm motion driven by M-HQSGr-RWKF artificial muscle, which could be observed detailedly in Movie S4, Supporting Information. E) Output stress and strain comparison between our M-HQSGr-RWKF artificial muscle and reported works. The details could be found in Table S3, Supporting Information.

α-helices formation. While keratin fiber is rewetting, the water molecules re-enter into the keratin interchain and form hydrogen bonds, which prompts the rapid transition from metastable β-sheets back to more disordered α-helices due to the principle of increase of entropy.

Afterwards, we quantitatively characterize the rearrangement of keratin fibril secondary structure by tracking the peak evaluation of the amide I Raman signal, which is deconvolved to α-helix and β-sheet in a separated specific peak range (see Table S2, Supporting Information for details). We monitor the fibril structure variation of both RWKF and M-HQSGr-RWKF via sub-dividing the tensile process into six states with stretching strains of 0%, 20%, 40%, 60%, 80%, and 100%. The local Raman spectral deconvolution for both two fibers at different stretching stages demonstrates that the β-sheet ratio gradually increases upon the continuous stretching (Figures S22 and S23, Supporting Information). As summarized in Figure 4E, M-HQSGr-RWKF presents a prominent increase from 28% to 79%, while RWKF exhibits an augment from 13% to 43%. The conspicuous transition of the keratin secondary structure indicates the possible strengthened actuation behavior. In addition, it has been reported that moisture-induced secondary structure transition can drive the actuation of keratin fiber. For example, Fratzl et al. studied the hydration mechanism of tendon collagen, which provides insights into how water can induce the conformation transition.[86,87] As

shown in Figure S24C, Supporting Information, RWKF tends to reach moisture adsorption saturation in 50 s with <3.00 mg water adsorption, while M-HQSGr-RWKF manifests over 12.00 mg water adsorption contributed by the consistent fiber mass. We summarized the response time and output stress for both RWKF and M-HQSGr-RWKF in Figure 4F,G., The M-HQSGr-RWKF could achieve an output stress of 16.7 MPa and a response time of 20 s, far surpassing that of 1.5 MPa and 40 s for RWKF. In this regard, M-HQSGr-RWKF is expected to demonstrate fabulous actuation performance.

2.5. Stimuli-Responsive Actuation of M-HQSGr-RWKF Artificial Muscle

The humidity-responsive actuation of M-HQSGr-RWKF artificial muscle has been schematically illustrated in **Figure 5**A. The initial fiber length is labeled as L_0. After continuous stretch and dehydration, the fiber length extends to L_1, accompanied with restoring specific quantities of β-sheets. Afterward, humidity stimulation triggered the fiber to recover its initial length L_0. The length difference is marked as ΔL, and the output strain is calculated as $\epsilon = \Delta L / L_0$. The actuation capability of these M-HQSGr-RWKF artificial muscles was qualitatively estimated by recording the geometries variation with humidity stimulus when exposed

to water spray at room temperature (Figure 5B), which indicates that M-HQSGr-RWKF artificial muscle manifests a 140% strain within a response time of only 20 s. Meanwhile, the fibrous artificial muscle also presents a high reversibility with gradually improved tensile strength (Figure S24D, Supporting Information). The self-reinforcing phenomenon of M-HQSGr-RWKF artificial muscle also further verifies the strengthening effect on keratin fibers of mechanical training.

After verifying the intrinsic actuation behavior of M-HQSGr-RWKF, we further demonstrate its potential as an artificial muscle with driving flower petal and forearm motion. The stimuli-responsive M-HQSGr-RWKF artificial muscle with reversible stretching/contracting properties can be used as localized "hinges" to control the folding process. After fixing petals along the longitude and latitude directions, the M-HQSGr-RWKF artificial muscle successfully drives the petals under humidity stimulation (Figure 5C, Movie S3, Supporting Information). Otherwise, M-HQSGr-RWKF with only 5 cm length and 5 mg weight have been assembled into an artificial muscle bundle and fixed between the articulatio humeri and the articulation cubiti in the polyethylene artificial forearm. The M-HQSGr-RWKF artificial muscle is also demonstrated to replace the biceps to drive arm bending movement, in which the "forearm" is ≈8 cm in length and 500 mg in weight (Figure 5D, Movie S4, Supporting Information). After applying extra moisture stimulation onto the fiber, the forearm bent 25° with an output work of 0.04 J in 40 s.

As shown in Figure 5E, compared with other natural muscle (skeletal muscle[57]), biomass artificial muscle (silk,[58] spider silk[59] and biomass lignin[60]), polymeric artificial muscle (polyethylene vinyl acetate (PEVA),[88] polyacrylic acid (PAA),[89] polyurethane-polyaniline (PU-PANi)[90] and polyhexamethylene adipamide (Nylon6,6)[91,92]), pneumatic artificial muscle (pleated pneumatic artificial muscles (PPAM),[93] origami-based vacuum pneumatic artificial muscles (OV-PAM)[94]) and CNTs-based artificial muscle counterparts,[95–97] the M-HQSGr-RWKF based system exhibits an ultrahigh actuation strain of 100% while maintaining distinguishing output stress. As a result, with the combination of the systematical analysis for the actuation behavior and demonstration for artificial muscle capability, M-HQSGr-RWKF could provide a bright avenue to customized actuation responsiveness toward broad biocompatible soft robotics or even bionic devices.

3. Conclusion

In summary, we fabricated an ultra-strong and ultra-tough M-HQSGr-RWKF with hundreds of meters in length through a continuous wet-spinning technique. HQSGr has been introduced to regulate the nontrivial secondary structure and polymeric aggregation conformation of keratin, inducing the reinforcement of the hybrid fiber with a tensile strength of 215.4 ± 5.2 MPa, in combination with the mechanical training post-treatment. The ultrahigh strength surpasses all previously reported WK fiber and is even comparable with degummed silk. In addition, M-HQSGr-RWKF has been demonstrated as a humidity-responsive artificial muscle, supported by the water-triggered transition of the keratin secondary structure. The enhanced mechanical strength and moisture adsorption capability remarkably improve the actuation performance to a toughness of 158.9 MJ m^{-3}, an output stress of

16.7 MPa, and a response time of 20 s. Furthermore, inspired by the motions observed in living organisms, M-HQSGr-RWKF artificial muscle has been demonstrated to drive biomimetic motion, such as petal closure and forearm bending. We anticipate that such ultra-strong and ultra-tough M-HQSGr-RWKF could shed light on the development of innovative bio-regenerated fiber manufacturing and stimuli-responsive applications for healthcare or personal protection.

4. Experimental Section

Regenerated Wool Keratin Extraction: The process for extracting regenerated wool keratin by reduction method entails several steps, including degreasing, dissolving, precipitation filtration, and freeze-drying.

Degreasing: First, the sheep wool was selected as the raw material of the experiment, and the wool was cut into 1 cm segments. Then, in order to remove the scales of the wool surface, the wool was immersed in 0.1 mmol mL^{-1} sodium carbonate (Greagent, Na$_2$CO$_3$, AR, ≥ 99.8%) solution for degreasing, bath ratio is 1:25.

Dissolution: Soak wool in 8 mmol mL^{-1} urea (Greagent, CO(NH$_2$)$_2$, AR, > 99%) solution, then 10% L-cysteine (Adamas, RG, > 97%) was added to break the disulfide bond. Then 0.02 mmol mL^{-1} sodium dodecyl sulfate (Greagent, SDS, AR, ≥ 90%) was added to enhance the dissolution effect. Finally, 1 mmol mL^{-1} sodium hydroxide (Greagent, NaOH, AR, ≥ 96%) solution was added to adjust the pH of the mixture to 11, and added the degreased wool with a bath ratio of 1:25. The mixture was mechanically stirred at 363 K for 4 h.

Precipitation and filtration: Filter the mixed solution obtained by dissolving the wool residue to get keratin solution, add 1 mmol mL^{-1} sodium sulfate (Adamas, Na$_2$SO$_4$, ACS, ≥ 99%) and hydrochloric acid (Greagent, HCl, AR, 36%–38%) solution to adjust the pH of keratin solution to 4. Then keratin was precipitated and filtered to get keratin solid. Finally, it was washed several times to remove residual urea in keratin.

Freeze-drying: The pure solid keratin was freeze-dried for 48 h to obtain keratin powder. As shown in Figure S3, Supporting Information, the extracted powder is high-quality keratin, which could be served as an ideal source for further RWKF fabrication.

Preparation of Various Graphene Materials: SGO was prepared by oxidation of natural graphite using modified Hummers.[98,99]

SRGO was prepared by the previously reported methods.[100] Hydrazine hydrate and ammonia were used as reducing agents and dispersants, respectively. In detail, 100 mL hydrazine hydrate (35 wt.%) and 22 ml ammonia (Greagent, AR, 25%–28 wt.%) were added to 100 ml 0.5 mg ml^{-1} SGO dispersion. Then the mixture was kept at 95 °C for 1 h to reduce the SRGO flakes.

The fabrication procedures of LGr were conducted according to the literature.[101] The large graphene oxide was thermally reduced to LGr by high-temperature heat treatment at 1473 K for 30 min.

HQSGr was synthesized according to the previously reported typical methods.[102] In the microwave environment, methane was used as a carbon source, and SiO$_2$/Si was discharged in the quartz tube to produce a corona, which was used to directly prepare HQSGr. The resulting graphene can float in the quartz tube-like "snow" for it to collect.

Continuous Wet-Spinning Process of RWKF and HQSGr-RWKF: The key of wet-spinning technique involves the preparation of precursor solution and the regulation of spinning parameters.

For pure WK spinning solution, keratin powder was dissolved in 0.3 mmol mL^{-1} sodium carbonate (Greagent, Na$_2$CO$_3$, AR, ≥ 99.8%)/sodium bicarbonate (Greagent, NaHCO$_3$, AR ≥ 99.5%) buffer solution. 10 wt.% DL-1,4-Dithiothreitol (Adamas, DTT, RG, 99%) was added to fully break the disulfide bond in keratin, and 10 wt.% SDS was added to assist in the dissolution of keratin and protect the reduced sulfhydryl group. After stirring for 12 h, the mixture was heated at 363 K for 1 h and placed at room temperature for 24 h.

For HQSGr-WK hybrid spinning solution, HQSGr was dispersed in SDS solution first, the other steps were consistent with the preparation process of spinning solution.

The prepared spinning solution was poured into the reaction kettle of the metering pump, and the reaction kettle was vacuumized for 5 min to remove the microbubbles in the spinning solution. The spinning solution was extruded from the spinneret using a metering pump at a rate of 0.6 cc min^{-1}. Here, the spinneret with an inner diameter of 100 µm and 20 holes was adopted. The drawing ratio of the primary fiber in the coagulation bath is $\lambda = 1$, which means that there is no drafting effect. The drawing ratio of the fiber in the oxidation bath is $\lambda = 1.2$, and the temperature of the dry tunnel is 313 K.

Mechanical Training: A mechanical training device was constructed that uniformly applies a tensile force along the fiber axis, and allows for manual adjustment of the stretch ratio and training rate during the training process. The maximum stretching ratio can reach 2.4, and the maximum training rate can reach 2 cycles s^{-1}. During the training, the fibers were loaded on two fixtures parallel to each other. By adjusting the motor speed, the fibers were trained with 10, 20, 30, 40, and 50 cycles within 60 s. The initial stretch ratio λ was 1.6, and the stretch ratio λ increased by 0.2 for every 10 cycles of training.

Preparation of Fibrous Artificial Muscle: One end of the fiber in the wet state was fixed, and the force along the fiber axial direction was applied to the other end. After 40 s, the fiber was dehydrated and dried. At this time, the length of the stretched fiber could be maintained by removing the force, and the artificial muscle was prepared.

Output Stress Measurement: Own test apparatus for measuring the output force was designed and developed. The Mark-10 dynamometer was sealed to ensure the uniform distribution of humidity in the testing environment. The humidifier was used to regulate the humidity in the confined space, and the fog output was 300 ml h^{-1}. The prepared artificial muscle was affixed onto the jig of the dynamometer, and the position of the jig was adjusted to keep the fiber tight. The resolution of the dynamometer was 5 mN. After the test is started, the output force during fiber contraction was recorded by holding the clamp steady.

Physicochemical Characterizations: X-ray diffraction patterns were obtained from a Bruker D8 advanced diffractometer with Cu-Kα radiation (wavelength dimension of 1.5406 Å), and the data were collected from 5° to 40° with a scan rate of 10° min^{-1}. The morphology and structure of the prepared fibers were collected by scanning electron microscopes (FEI Scios) with an accelerating voltage of 10.0 kV. X-ray photoelectron spectroscopy (XPS) was collected through an ESCALAB 250Xi spectrophotometer using a monochromatic Al Kα X-ray source (ThermoFisher Scientific). The Fourier-transform infrared spectroscopy (FT-IR) was carried out in an absorption mode (Bruker Tensor 27). The Raman spectroscopy was performed by using a LabRAM HR800 (JobinYvon) instrument with a 785 nm incident radiation and a 50× aperture. ^{13}C solid-state NMR spectra were collected at 400 MHz on a Bruker Advance III HD 400 WB spectrometer, and the Larmor frequency was 100.6 MHz. WK sample filled in a 3.2 mm diameter ZrO$_2$ rotor with spinning at 10 kHz frequency. The chemical shifts of ^{13}C spectra were reported with reference to tetramethylsilane (TMS) and CH peak from Adamantane. SAXS measurements were performed on a beamline (BL19U2) at Shanghai Synchrotron Radiation Facility. The wavelength dimension of the X-ray was 1.033 Å and the distance between the detector and the sample was 2205 mm. The resulting analysis of the SAXS patterns was performed by Fit2D software.

Supporting Information

Supporting Information is available from the Wiley Online Library or from the author.

Acknowledgements

Conflict of Interest

The authors declare no conflict of interest.

Data Availability Statement

The data that support the findings of this study are available on request from the corresponding author. The data are not publicly available due to privacy or ethical restrictions.

Keywords

[1] H. M. Manohara, S. S. Nayak, G. Franklin, S. K. Nataraj, D. Mondal, *Green Chem.* **2021**, *23*, 8305.

[2] S. Khandaker, M. M. Bashar, A. Islam, M. T. Hossain, S. H. Teo, M. R. Awual, *Renewable Sustainable Energy Rev.* **2022**, *157*, 112051.

[3] Editorial. *Nat. Rev. Mater.* **2022**, *7*, 67.

[4] V. Sacha, *Science* **2020**, *370*, 2.

[5] T. Li, J. W. Song, X. P. Zhao, Z. Yang, G. Pastel, S. M. Xu, C. Jia, J. Q. Dai, C. J. Chen, A. Gong, F. Jiang, Y. G. Yao, T. Z. Fan, B. Yang, L. Wågberg, R. G. Yang, L. B. Hu, *Sci. Adv.* **2018**, *4*, 9.

[6] H. Tu, M. Zhu, B. Duan, L. Zhang, *Adv. Mater.* **2021**, *33*, 2000682.

[7] S. Zhou, K. Jin, M. J. Buehler, *Adv. Mater.* **2021**, *33*, 2003206.

[8] K. Mihaly, *Nature* **1960**, *188*, 251.

[9] M. Daniele, G. Stéphane, J. Guan, A. Ferri, F. Salaün, *Environ. Chem. Lett.* **2019**, *17*, 1787.

[10] N. Yan, X. Chen, *Nature* **2015**, *524*, 155.

[11] L. Y. Jeffery, R. C. Brian, V. Arjan, *Nat. Rev. Mater.* **2018**, *3*, 11.

[12] Z. Z. Shao, V. Fritz, *Nature* **2002**, *418*, 741.

[13] Q. Wang, S. J. Ling, Q. Z. Yao, Q. Y. Li, D. B. Hu, Q. Dai, D. A. Weitz, D. L. Kaplan, M. J. Buehler, Y. Y. Zhang, *ACS Mater. Lett.* **2020**, *2*, 153.

[14] F. Allafi, M. S. Hossain, J. Lalung, M. Shaah, A. Salehabadi, M. I. Ahmad, A. Shadi, *J. Nat. Fibers* **2020**, *19*, 497.

[15] B. Wang, W. Yang, J. McKittrick, A. M. Marc, *Prog. Mater. Sci.* **2016**, *76*, 229.

[16] N. R. Sun, H. Wu, X. Z. Shen, C. H. Deng, *Adv. Funct. Mater.* **2019**, *29*, 1900253.

[17] A. K. Brad, C. P. Amy, P. S. Alia, J. S. Andrew, C. H. Sarah, *Prog. Mater. Sci.* **2018**, *91*, 1.

[18] S. J. Ling, Z. Qin, C. Li, W. Huang, D. L. Kaplan, M. J. Buehler, *Nat. Commun.* **2017**, *8*, 1387.

[19] J. Ren, Y. Wang, Y. Yao, Y. Wang, X. Fei, P. Qi, S. Lin, D. L. Kaplan, M. J. Buehler, S. J. Ling, *Chem. Rev.* **2019**, *119*, 12279.

**ADVANCED
SCIENCE NEWS**

www.advancedsciencenews.com

**ADVANCED
FUNCTIONAL
MATERIALS**

www.afm-journal.de

[20] B. A. Tamara, D. Elise, S. Thomas, *Adv. Mater.* **2018**, *30*, 1704636.

[21] Y. Shen, A. Levin, A. Kamada, Z. Toprakcioglu, M. R. Garcia, Y. F. Xu, T. P. J. Knowles, *ACS Nano* **2021**, *15*, 5819.

[22] Y. Y. Han, Z. X. Lin, J. J. Zhou, G. Yun, R. Guo, J. J. Richardson, F. Caruso, *Angew. Chem., Int. Ed.* **2020**, *59*, 15618.

[23] H. Tu, R. Yu, Z. F. Lin, L. Zhang, N. B. Lin, W. D. Yu, X. Y. Liu, *Adv. Funct. Mater.* **2016**, *26*, 9032.

[24] S. Keten, Z. Xu, B. Ihle, M. J. Buehler, *Nat. Mater.* **2010**, *9*, 359.

[25] S. G. Wiedemann, M. J. Yan, B. K. Henry, C. M. Murphy, *J. Clean Prod.* **2016**, *122*, 121.

[26] S. Ranford, P. Swan, C. V. Koten, *Sci. Rep.* **2022**, *12*, 768.

[27] K. T. Sundari, P. Ramalakshmi, *Asian Rev. Social Sci.* **2018**, *7*, 3.

[28] X. T. Sun, X. Wang, F. Q. Sun, M. W. Tian, L. J. Qu, P. Perry, H. Owens, X. Q. Liu, *Adv. Mater.* **2021**, *33*, 2105174.

[29] J. W. Loh, X. Y. Goh, T. T. N. Phuc, B. T. Quoc, Z. Y. Ong, H. M. Duong, *J. Polym. Environ.* **2021**, *30*, 681.

[30] W. Y. Tang, B. Tang, W. L. Bai, E. Pakdel, J. F. Wang, X. G. Wang, *J. Clean Prod.* **2022**, *366*.

[31] X. Mi, B. N. Mu, W. Li, H. L. Xu, Y. Q. Yang, *ACS Sustainable Chem. Eng.* **2020**, *8*, 1396.

[32] B. N. Mu, F. Hassan, Y. Q. Yang, *Green Chem.* **2020**, *22*, 1726.

[33] R. L. Wormell, F. Happey, *Nature* **1949**, *163*, 2.

[34] L. Cera, G. M. Gonzalez, Q. Liu, S. Choi, C. O. Chantre, J. Lee, R. Gabardi, M. C. Choi, K. Shin, K. K. Parker, *Nat. Mater.* **2021**, *20*, 242.

[35] I. Bianco, R. Gerboni, G. Picerno, G. A. Blengini, *Resources* **2022**, *11*, 41.

[36] J. P. Andrew, S. C. Jeffrey, G. H. Mickey, *Biomacromolecules* **2009**, *10*, 8.

[37] M. Anton, *Prog. Polym. Sci.* **2002**, *27*, 61.

[38] F. Happey, T. P. Macrae, G. J. Weston, *Nature* **1953**, *172*, 2.

[39] M. G. Dobb, *Nature* **1964**, *202*, 2.

[40] I. Macarthur, *Nature* **1943**, *152*, 38.

[41] E. J. Ambrose, A. Elliott, *Nature* **1949**, *163*, 859.

[42] R. B. Bruce, P. M. Thomas, A. D. P. David, *Proc. Nat. Acad. Sci. U. S. A.* **1986**, *83*, 5.

[43] A. R. B. Skertchly, *Nature* **1958**, *181*, 2.

[44] Y. W. Liu, S. Jing, D. Carvalho, J. J. Fu, M. Martins, P. A. Cavaco, *ACS Sustainable Chem. Eng.* **2021**, *9*, 4102.

[45] A. Kamada, A. Levin, Z. Toprakcioglu, Y. Shen, V. Lutz-Bueno, K. N. Baumann, P. Mohammadi, M. B. Linder, R. Mezzenga, T. P. J. Knowles, *Small* **2020**, *16*, 1904190.

[46] X. Ye, A. J. Capezza, S. Davoodi, X. F. Wei, R. L. Andersson, A. Chumakov, S. V. Roth, M. Langton, F. Lundell, M. S. Hedenqvist, C. Lendel, *ACS Nano* **2022**, *16*, 12471.

[47] I. Su, N. Narayanan, M. A. Logrono, K. Guo, A. Bisshop, R. Muhlethaler, T. Saraceno, M. J. Buehler, *Proc. Natl. Acad. Sci. USA* **2021**, *118*.

[48] I. H. Kim, T. Yun, J. E. Kim, H. G. Yu, S. P. Sasikala, K. E. Lee, S. H. Koo, H. wang, H. J. Jung, J. Y. Park, H. S. Jeong, S. O. Kim, *Adv. Mater.* **2018**, *30*, 1870298.

[49] H. I. Mohammad, A. Shaila, A. U. Mohammad, V. A. Daria, S. N. Kostya, N. Karim, *Adv. Funct. Mater.* **2022**, *32*, 2205723.

[50] C. D. Melik, V. Mert, T. Mauricio, *Adv. Funct. Mater.* **2017**, *28*, 1704990.

[51] X. Y. Huang, C. Y. Zhi, Y. Lin, H. Bao, G. N. Wu, P. K. Jiang, Y. W. Mai, *Mater. Sci. Eng. R Rep.* **2020**, *142*.

[52] L. Huang, N. Yi, Y. Wu, Y.i Zhang, Q. Zhang, Y. Huang, Y. Ma, Y. Chen, *Adv. Mater.* **2013**, *25*, 2224.

[53] S. James, *Nat. Photonics* **2019**, *13*, 731.

[54] M. K. Shin, B. Lee, S. H. Kim, J. A. Lee, G. M. Spinks, S. Gambhir, G. G. Wallace, M. E. Kozlov, R. H. Baughman, S. J. Kim, *Nat. Commun.* **2012**, *3*, 650.

[55] S. R. Tan, M. R. Islam, H. X. Li, A. Fernando, S. Afroj, N. Karim, *Adv. Sensor Res.* **2022**, *1*, 2200010.

[56] S. Afroj, L. Britnell, T. Hasan, D. V. Andreeva, K. S. Novoselov, N. Karim, *Adv. Funct. Mater.* **2021**, *31*, 2107407.

[57] C. Gotti, A. Sensini, A. Zucchelli, R. Carloni, M. L. Focarete, *Appl. Mater. Today* **2020**, *20*, 100772.

[58] T. J. Jia, Y. Wang, Y. Dou, Y. Li, M. J. Andrade, R. Wang, S. Fang, J. Li, Z. Yu, R. Qiao, Z. Liu, Y. Cheng, Y. Su, M. J. Majid, R. H. Baughman, D. Qian, Z. F. Liu, *Adv. Funct. Mater.* **2019**, *29*, 1808241.

[59] A. Ingi, D. Ali, S. Vasav, A. B. Todd, *J. Exp. Biol.* **2009**, *212*, 1990.

[60] Z. K. Tu, W. F. Liu, J. Wang, X. Q. Qiu, J. H. Huang, J. X. Li, H. M. Lou, *Nat. Commun.* **2021**, *12*, 2916.

[61] K. Amal, A. A. Ali, S. T. George, M. Bernhard, C. Matthew, V. Libor, *J. Phys. Chem. C* **2012**, *116*, 2858.

[62] M. D. Watson, I. Peran, J. Zou, O. Bilsel, D. P. Raleigh, *Biochemistry* **2017**, *56*, 1085.

[63] S. Wei, X. Q. Zou, J. Y. Tian, H. Huang, W. Guo, Z. Chen, *J. Am. Chem. Soc.* **2019**, *141*, 20335.

[64] B. Maria, E. D. Dan, P. Crisan, F. Radu, M. Claudiu, B. Bernhard, M. Martin, *J. Phys. Chem. B* **2009**, *113*, 9.

[65] J. D. Melinda, M. Nicky, C. M. Rachel, *Phys. Chem. Chem. Phys.* **2003**, *5*, 2894.

[66] D. Jain, A. Y. Stark, P. H. Niewiarowski, T. Miyoshi, A. Dhinojwala, *Sci. Rep.* **2015**, *5*, 9594.

[67] K. Wang, R. Li, J. H. Ma, Y. K. Jian, J. N. Che, *Green Chem.* **2016**, *18*, 476.

[68] C. Gaidau, D. G. Epure, C. E. Enascuta, C. Carsote, C. Sendrea, N. Proietti, W. Y. Chen, H. B. Gu, *J. Clean Prod.* **2019**, *236*, 117586.

[69] S. T. Lina, J. Liua, X. Y. Liua, X. H. Zhao, *Proc. Nat. Acad. Sci. U. S. A.* **2019**, *116*, 10244.

[70] T. Matsuda, R. Kawakami, R. Namba, T. Nakajima, J. P. Gong, *Science* **2019**, *363*, 504.

[71] T. Shu, Z. C. Lv, C. T. Chen, G. X. Gu, J. Ren, L. T. Cao, Y. Pei, S. J. Ling, D. L. Kaplan, *Small* **2021**, *17*, 2102660.

[72] L. Rintoul, E. A. Carter, S. D. Stewart, P. M. Fredericks, *Biopolymers* **2000**, *57*, 19.

[73] A. G. Kikhney, D. I. Svergun, *FEBS Lett.* **2015**, *589*, 2570.

[74] C. J. Moger, R. Barrett, P. Bleuet, D. A. Bradley, R. E. Ellis, E. M. Green, K. M. Knapp, P. Muthuvelu, C. P. Winlove, *Osteoarthritis Cartilage* **2007**, *15*, 682.

[75] F. T. Andreas, W. Rulland, *Macromolecules* **2000**, *33*, 5.

[76] X. Y. Li, F. Tian, X. P. Gao, F. G. Bian, X. H. Li, J. Wang, *New Carbon Mater.* **2017**, *32*, 130.

[77] T. G. David, W. J. Lynn, *Macromolecules* **1997**, *30*, 8.

[78] G. Beaucage, *J. Appl. Crystallogr.* **1996**, *29*, 134.

[79] G. Beaucage, *J. Appl. Crystallogr.* **1995**, *28*, 717.

[80] L. H. Lu, W. Chen, *Adv. Mater.* **2010**, *22*, 3745.

[81] D. B. Liu, A. Tarakanova, C. C. Hsu, M. Yu, S. M. Zheng, L. T. Yu, J. Liu, Y. M. He, D. J. Dunstan, M. J. Buehler, *Sci. Adv.* **2019**, *5*, eaau9183.

[82] A. N. Zelikin, C. Ehrhardt, A. M. Healy, *Nat. Chem.* **2016**, *8*, 997.

[83] T. Jiang, W. Y. Qiu, Z. Y. Li, X. Ye, Y. H. Liu, Y. S. Li, X. H. Wang, J. W. Zhong, X. Qian, L. W. Lin, *Adv. Funct. Mater.* **2022**, *32*, 2107985.

[84] T. Zheng, P. P. Abadi, J. Seo, B. H. Cha, B. Miccoli, Y. C. Li, K. Park, S. Park, S. J. Choi, R. Bayaniahangar, D. Zhang, S. H. Lee, C. K. Lee, A. Khademhosseini, S. R. Shin, *ACS Appl. Mater. Interfaces* **2019**, *11*, 20615.

[85] A. Miserez, S. S. Wasko, C. F. Carpenter, J. H. Waite, *Nat. Mater.* **2009**, *8*, 910.

[86] H. C. Quan, D. Kisailus, M. A. Meyers, *Nat. Rev. Mater.* **2020**, *6*, 264.

[87] A. Masic, L. Bertinetti, R. Schuetz, S. W. Chang, T. H. Metzger, M. J. Buehler, P. Fratzl, *Nat. Commun.* **2015**, *6*, 5942.

[88] J. Fan, G. Li, *RSC Adv.* **2017**, *7*, 1127.

[89] R. C. Christine, C. Corentin, N. Manoj, L. C. David, R. H. Roy, G. Martin, *Biomaterials* **2009**, *30*, 1205.

ADVANCED
SCIENCE NEWS

www.advancedsciencenews.com

ADVANCED
FUNCTIONAL
MATERIALS

www.afm-journal.de

[90] J. K. Chang, M. T. Lee, W. T. Tsai, M. J. Deng, I. W. Sun, *Chem. Mater.* **2009**, *21*, 2688.

[91] C. S. Haines, M. D. Lima, N. Li, G. M. Spinks, J. Foroughi, J. Madden, S. H. Kim, S. Fang, M. Andrade, G. Fatma, O. Göktepe, S. M. Mirvakili, S. Naficy, L. Xavier, O. Jiyoung, E. K. Mikhail, S. J. Kim, X. Xu, B. J. Swedlove, G. G. Wallace, R. H. Baughman, *Science* **2014**, *343*, 868.

[92] J. K. Mu, M. J. Andrade, S. L. Fang, X. M. Wang, E. L. Gao, N. Li, S. H. Kim, H. Z. Wang, C. Y. Hou, Q. H. Zhang, M. F. Zhu, D. Qian, H. B. Lu, K. Dharshika, T. Sepehr, J. Foroughi, G. Spinks, H. Kim, T. H. Ware, H. J. Sim, D. Y. Lee, Y. W. Jang, S. J. Kim, R. H. Baughman, *Science* **2019**, *365*, 150.

[93] M. Meller, J. Chipka, A. Volkov, M. Bryant, E. Garcia, *Bioinspir. Biomim.* **2016**, *11*, 065004.

[94] J. G. Lee, H. Rodrigue, *Soft Rob.* **2019**, *6*, 109.

[95] J. A. Lee, Y. T. Kim, G. M. Spinks, D. Suh, X. Lepro, M. D. Lima, R. H. Baughman, S. J. Kim, *Nano Lett.* **2014**, *14*, 2664.

[96] J. A. Lee, N. Li, C. S. Haines, K. J. Kim, X. Lepro, R. R. Ovalle, S. J. Kim, *Adv. Mater.* **2017**, *29*, 1700870.

[97] M. Ren, J. Qiao, Y. L. Wang, K. J. Wu, L. Z. Dong, X. F. Shen, H. C. Zhang, W. Yang, Y. L. Wu, Z. Z. Yong, W. Chen, Y. Y. Zhang, J. T. Di, Q. W. Li, *Small* **2021**, *17*, 2006181.

[98] S. H. J. William, E. O. Richard, *J. Am. Chem. Soc.* **1958**, *80*, 1339.

[99] M. D. Ayrat, M. T. James, *ACS Nano* **2014**, *8*, 9.

[100] S. Sasha, A. D. Dmitriy, D. P. Richard, A. K. Kevin, K. Alfred, Y. Y. Jia, Y. Wu, T. N. SonBinh, S. R. Rodney, *Carbon* **2007**, *45*, 1558.

[101] L. Rosanna, F. Stefano, T. Sun, L. Paolo, B. Alessandro, L. Silvano, *J. Am. Chem. Soc.* **2011**, *133*, 17315.

[102] Y. Y. Sun, L. W. Yang, K. L. Xia, H. Z. Liu, D. Han, Y. Y. Zhang, J. Zhang, *Adv. Mater.* **2018**, 1803189.